A numerical model for the transport and drying of solutions in thin porous media

Colloids and Surfaces A: Physicochemical and Engineering Aspects 682 (2024) 132839

Contents lists available at ScienceDirect

Colloids and Surfaces A: Physicochemical and Engineering Aspects

journal homepage: www.elsevier.com/locate/colsurfa

A numerical model for the transport and drying of solutions in thin porous media — Coffee-stain effect and solute ring formation

S. Wang, A.A. Darhuber *

Fluids & Flows Group, Department of Applied Physics, Eindhoven University of Technology, The Netherlands

GRAPHICAL ABSTRACT

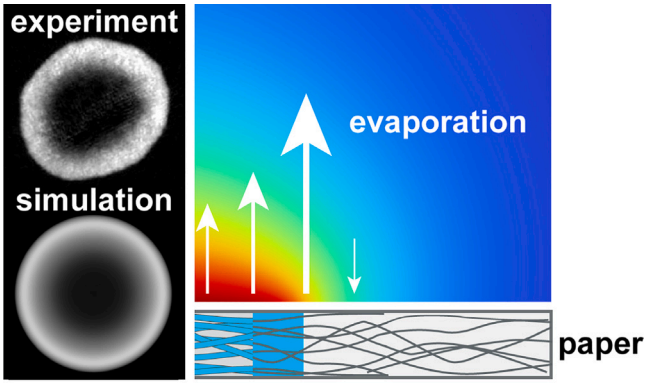

ARTICLE INFO

Keywords:
Inkjet printing
Co-solvents
Multi-component flow
Darcy flow
Thin porous media
Coffee stain effect

ABSTRACT

We have developed a comprehensive numerical model for the transport and drying of solutions in thin porous media that consist of permeable fibers such as paper. We explicitly account for the gas-phase transport dynamics. Moreover, we introduce an empirical relation for the concentration- and molecular-weight dependence of the pore-fiber transport rate of the solutes. These two key elements enable us for the first time to realistically model two important phenomena relevant to inkjet printing technology. The first is the equivalent of the coffee-stain effect for dilute solutions in porous media. The second is the formation of solute rings for concentrated aqueous mixtures of compounds with a molecular weight significantly above that of water. Whereas the first is governed by spatially non-uniform solvent evaporation, the second case is dominated by solvent-mediated pore-fiber transport. We achieved a good qualitative agreement with the available experimental data.

1. Introduction

The formation of a coffee stain at the perimeter of an evaporating solution droplet resting with pinned contact lines on an impermeable surface is a well-known phenomenon [1]. Dou & Derby, Huang et al. and Li et al. studied coffee-stain formation *on top of* porous media [2–4], for which no solute transport inside the porous media occurs. Coffee stains are usually not observed after deposition of dilute solution droplets that imbibe, spread and dry *inside* porous media. This is typically caused by adsorption effects that deplete the solute near the perimeter of the wet zone due to chromatographic retention [5]. Notable exceptions were found for wet porous media of *finite* dimensions [6–9] or heterogeneous, chemically-patterned media, where a hydrophobic barrier confines liquid to certain regions [9–15].

An important technological application of solution transport in porous media is inkjet printing. The main constituents of inkjet inks

* Corresponding author.
E-mail address: a.a.darhuber@tue.nl (A.A. Darhuber).

https://doi.org/10.1016/j.colsurfa.2023.132839
Received 31 August 2023; Received in revised form 18 November 2023; Accepted 20 November 2023
Available online 24 November 2023

are typically water as an environmentally safe solvent, colorants, surfactants as well as so-called co-solvents [16]. The latter are polar liquids of low volatility such as glycerol, with a concentration up to 50% [16]. Their primary purpose is the prevention of inkjet nozzle clogging [16–18], among others [18–20]. Wijburg et al. [21] investigated the transport of non-dilute, aqueous co-solvent solutions in paper substrates and observed the occurrence of solute rings after drying.

Our main interest is to understand the redistribution dynamics of solutes contained in water-based inks after printing, and specifically the formation of coffee-stains and solute rings inside thin porous media. For this purpose, we studied the transport processes after droplet deposition during the drying phase of paper sheets that have an initial maximum moisture content MC comparable to the maximum holding capacity of paper, which is approximately 1.0 kg water/1 kg of dry paper [22]. The redistribution of solid-phase solutes such as typical dyes is essentially arrested when the moisture content falls below a threshold of $MC_{\mathrm{crit}} \approx 0.07$. Below MC_{crit} there is essentially only adsorbed water left in the paper sheet, but the mobile liquid-phase water has evaporated. Therefore, we consider only liquid-phase ink transport in our model, i.e. a combination of Darcy flow and liquid-phase diffusion and dispersion. This approach is obviously also suitable for solutes that remain in a liquid state after water evaporation such as typical co-solvents. Their redistribution is not arrested when most of the water has evaporated, but it markedly slows down due to the sensitive dependence of viscosity on solvent concentration and of the effective permeability on liquid content.

Paper is a thin porous medium consisting mainly of permeable cellulose fibers [23]. Usually the presence of permeable fibers is not explicitly considered in the literature on paper drying [24–29]. This is not necessary, because the timescale for pore-fiber equilibration, which is on order of 1 s for liquid-phase water in unsized paper, is typically much shorter than the drying time. In contrast, in the final stage of paper drying below MC_{crit}, this equilibration time is much longer (e.g. 300 s in [30]). Therefore, Bandyopadhyay et al. presented a model, assuming water vapor diffusion is the dominant transport mechanism, that does take the presence of permeable fibers explicitly into account [30]. Zapata et al. improved on this model by also considering heat transfer [31]. They assumed the pore-fiber transport rate to be an empirical, linear relation with a constant time-scale, which implies that its validity is restricted to modest variations of the moisture content.

In our case, the initial moisture distribution is not spatially uniform, but highly heterogeneous, due to the localized deposition of an ink droplet on a paper sheet. Venditti et al. presented a model for the transport and evaporation of dilute solutions of surface-active compounds in paper. They took the presence of permeable fibers into account, although the pore-fiber equilibration time is short for dilute solutions [32]. This is an essential element, however, because the fibers can take up both solvent and solute that become essentially immobilized temporarily, which greatly affects the transient moisture profile and the solute distribution upon droplet imbibition [32].

Venditti et al. approximated the evaporative solvent flux j_{ev} by a global mass transfer relation

$$j_{\mathrm{ev}} = -k_{\infty}\left[\rho_{\mathrm{H_2O}}(z=0) - \rho_{\mathrm{H_2O}}(z\to\infty)\right], \tag{1}$$

where, $\rho_{\mathrm{H_2O}}(z=0)$ and $\rho_{\mathrm{H_2O}}(z\to\infty)$ are the water vapor concentrations at the paper surface $z=0$ and in the ambient atmosphere, respectively, and k_{∞} is a mass transfer coefficient. Expressions of this type are commonly used in the drying literature [24,25,27–29,31,33–35]. Eq. (1) can properly account for the overall mass loss, but cannot reproduce its position dependence near boundaries of wet zones. Therefore, we adopt the diffusion-limited evaporation model

$$j_{\mathrm{ev}} = D_{\mathrm{H_2O}}\frac{\partial \rho_{\mathrm{H_2O}}}{\partial z}(z=0) \tag{2}$$

used e.g. by Murali et al. [36], where $D_{\mathrm{H_2O}}$ is the diffusion coefficient of water vapor in air. We solve for flow, heat transfer and water vapor transport in the gas phase, coupled to the flow, heat and mass transfer inside the paper sheet. This yields the correct position dependence of the evaporative flux, even at abrupt wet zone boundaries, which is a key ingredient to study coffee-stain and solute-ring formation.

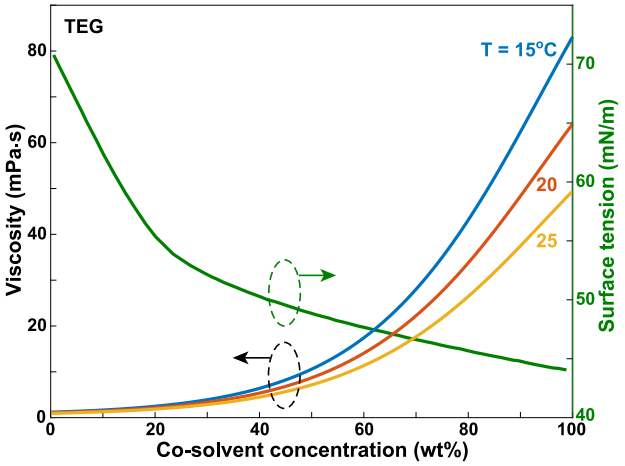

Fig. 1. Viscosity μ_{TEG} and surface tension σ_{TEG} as a function of composition for aqueous TEG solutions [40].

To account for the micro-structure of paper, we applied a dual-medium description [32], which allows for transport of liquid and solutes between the inter-fiber and intra-fiber porespaces. Typical co-solvents have a molecular weight (MW) between 50 and 300. If their MW is below the cut-off value for penetration of the cellulose fiber walls [37–39], they can migrate into the cellulose fibers. Wijburg et al. found that this pore-fiber migration rate is highly sensitive to the co-solvent MW and the local co-solvent concentration [21]. They ascribed the latter effect to water acting as a plasticizer of the cellulose fiber walls. We extended the pore-fiber exchange model introduced in [32] to account for both this plasticization effect and the dependence on solute MW. We performed a systematic parameter study and obtained good qualitative agreement between our simulations and the experiments regarding coffee-stain formation by Nilghaz et al. [9] as well as the co-solvent ring formation experiments in [21].

2. Material properties

The material properties of mixtures and solutions are generally concentration dependent. For the case of aqueous co-solvent solutions, the parameters that are most sensitive to composition variations are surface tension, viscosity and saturated vapor pressure. For most of our simulations, we use the properties of tetra(ethylene glycol) (TEG)-water mixtures as a representative co-solvent solution. Fig. 1 shows the viscosity μ_{TEG} and surface tension σ_{TEG} of TEG solutions, which vary by factors of approximately 50 and 0.6, respectively, over the composition range. Analytical representations of μ_{TEG} and σ_{TEG} are provided in the Supplementary Information, along with material properties of other common co-solvents. Many properties are only weakly composition dependent, such that we substitute values for pure substances for convenience. These approximations are also listed in the Supplementary Information.

2.1. Water activity

Both paper and co-solvents are hygroscopic materials that absorb appreciable quantities of water depending on the relative humidity r_h of the surrounding gas phase [41,42]. For binary mixtures of water and typical co-solvents, the Van Laar relation [43,44]

$$\ln\gamma_w = A_{21}\left(\frac{A_{12}x_{\mathrm{cs}}}{A_{12}x_{\mathrm{cs}} + A_{21}x_w}\right)^2 \tag{3}$$

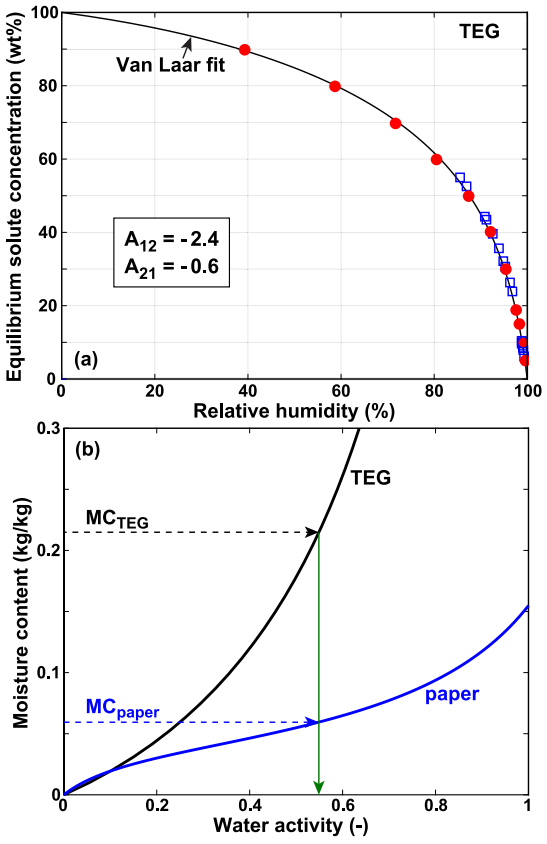

Fig. 2. (a) Equilibrium co-solvent concentration of an aqueous solution of TEG as a function of relative humidity. The filled red circles and the open squares represent experimental data from Refs. [41,42], respectively. The solid line is a fit according to Eq. (3). (b) Moisture isotherms for TEG (black solid line) and paper (blue solid line, GAB parameters $M_0 = 0.04$, $k = 0.75$ and $C = 10$).

can represent the equilibrium mixture composition as a function of r_h quite well, provided the coefficients A_{12} and A_{21} are treated as adjustable parameters. Here, γ_w is the solvent activity coefficient [45] and x_{cs} and $x_w = 1 - x_{cs}$ are the mole fractions of co-solvent and water, respectively. Fig. 2 shows an example for TEG with fitted values $A_{12} = -2.4$ and $A_{21} = -0.6$. Analogous fits for selected other co-solvents are given in the Supplementary Information.

In equilibrium, the co-solvent weight fraction

$$w_{cs} \equiv \frac{m_{cs}}{m_{cs} + m_w}, \tag{4}$$

where m_w and m_{cs} represent the mixture masses of water and co-solvent, respectively, can be translated into a moisture content (with units kg of water/kg of co-solvent)

$$MC_{cs} \equiv \frac{m_w}{m_{cs}} = \frac{1}{w_{cs}} - 1, \tag{5}$$

which is plotted as the black solid line in Fig. 2(b). It follows from Eq. (5) that

$$x_w = \frac{1}{1 + \frac{MW_w}{MW_{cs}} \frac{1}{MC_{cs}}} = 1 - x_{cs}. \tag{6}$$

For paper, the Guggenheim–Anderson–De Boer (GAB) isotherm

$$MC_{paper} = \frac{M_0 C k a_w}{(1 - k a_w)(1 - k a_w + C k a_w)} \tag{7}$$

can represent the moisture sorption behavior as a function of water activity

$$a_w \equiv \frac{\rho_{H_2O}}{\rho_{sat}} \tag{8}$$

well. Here, M_0, k and C are adjustable parameters, ρ_{H_2O} is the water vapor mass density in the gas phase and ρ_{sat} its saturated value. A typical example of a GAB isotherm is shown as the blue solid line in Fig. 2(b).

To the best of our knowledge, the moisture isotherms of paper sheets containing various quantities of co-solvents per unit area are not available in the literature. Therefore, we make two assumption to arrive at a relation between water activity, solution mass and composition. Firstly, we assume that as far as their moisture sorption behavior is concerned, paper and co-solvent do not interact, i.e. the moisture sorption capacity of paper is not affected by the presence of and contact with co-solvents and vice versa. Secondly, we assume that the chemical potential of water is uniform, i.e. it has the same value in both the paper phase and the solution phase.

When solving the dynamic equations for liquid transport in paper, the quantity of co-solvent and water per unit area, $\Theta_{tot,cs}$ and $\Theta_{tot,w}$, are known. For solving the gas-phase dynamics, the water activity at the paper–gas interface is required. Eq. (7) can be inverted [46,47] to yield

$$a_w[(MC)_{paper}] = \frac{2 + (\frac{M_0}{MC_{paper}} - 1)C - \sqrt{\left[\frac{CM_0}{MC_{paper}}\right]^2 + (4 - 2C)C\frac{M_0}{MC_{paper}} + C^2}}{2k(1 - C)}. \tag{9}$$

The condition of local thermodynamic equilibrium then can be formulated as

$$a_w[(MC)_{paper}] = a_w[(MC)_{cs}] = \gamma_w x_w \tag{10}$$

and correspondingly the total local areal density of moisture is assigned to the paper phase and the co-solvent phase according to

$$\rho_{paper} MC_{paper} + \Theta_{tot,cs} MC_{cs} = \Theta_{tot,w}. \tag{11}$$

Here, ρ_{paper} is the grammage or areal mass density of the porous medium. Thus, Eqs. (10), (11) represent two equations for the two unknowns MC_{paper} and MC_{cs}, which we solved numerically and from which a_w as a function of $\Theta_{tot,cs}$ and $\Theta_{tot,w}$ can be determined using Eq. (10).

3. Theoretical model

3.1. Liquid transport in paper

We adopted and extended the model of [32], rewritten for an axisymmetric system. All quantities are assumed uniform in the thickness direction of the thin porous medium. This implicitly assumes that the timescale of transport in the thickness direction is much shorter than for the in-plane direction, which is consistent with the experimental systems we will compare to. The mass conservation equation for the liquid in the inter-fiber pores of the paper substrate is given by

$$\frac{\partial \Theta}{\partial t} + \rho_{liq} t_p \frac{1}{r}\frac{\partial}{\partial r}(rv) = j_{ev,p} - s_{pf}, \tag{12}$$

where Θ denotes the liquid content in the inter-fiber pores (units kg/m^2), t_p the substrate thickness, ρ_{liq} the mass density of the liquid mixture, v the radial Darcy velocity, $j_{ev,p}$ the evaporative flux from inter-fiber pores and s_{pf} the pore-fiber transport rate, respectively. The radial Darcy velocity v is given by

$$v = -\frac{K}{\mu}\left(\frac{\partial p}{\partial \Theta}\frac{\partial \Theta}{\partial r} + \frac{\partial p}{\partial c}\frac{\partial c}{\partial r}\right). \tag{13}$$

For the effective permeability K of the porous medium, we adopt the Van Genuchten relation as detailed in [22,32]. Similarly, we adopt a Van Genuchten relation for the capillary pressure p, which is determined by Θ and the solute concentration in the pores c

$$p = p_g(c)\left[\left(\frac{\Theta}{\Theta_{max}}\right)^{-\frac{1}{m_g}} - 1\right]^{\frac{1}{n_g}}. \tag{14}$$

Here, $\Theta_{\max}$ denotes the maximum holding capacity of the inter-fiber pores and n_g and m_g are constants. The prefactor $p_g(c)$ is a function of surface tension σ_{lv} and is thus composition dependent [32,48,49]

$$p_g(c) \equiv p_g(0)\frac{\sigma_{lv}(c)\cos\alpha(c)}{\sigma_{lv}(c=0)\cos\alpha(c=0)}\,, \tag{15}$$

where σ_{lv} is the liquid–air interfacial tension of the mixture and α is the contact angle on the pore walls.

We assume the permeability of the intra-fiber pores to be so small that the liquid can be considered as effectively immobile. Hence, the liquid content in the fibers Θ_f only changes due to the evaporative flux $j_{ev,f}$ and pore-fiber transport

$$\frac{\partial\Theta_f}{\partial t} = j_{ev,f} + s_{pf}\,. \tag{16}$$

We assume the capillary pressure in the intra-fiber pores to be higher than in the inter-fiber pores:

$$p_f = a_f\, p_g(c_f)\left[\left(\frac{\Theta_f}{\Theta_{\mathrm{f,max}}}\right)^{-\frac{1}{m_g}} - 1\right]^{\frac{1}{n_g}}. \tag{17}$$

Here, $\Theta_{\mathrm{f,max}}$ denotes the maximum holding capacity of the intra-fiber pores and a_f is a constant. For the commercial, inkjet-optimized printing paper used in the experiments in [21], it holds to good approximation that $\Theta_{\max} = \Theta_{\mathrm{f,max}}$ and that $\alpha(c) = \alpha_f(c) = 0$.

Fig. 3(a) illustrates the capillary pressures in the pores $p(\Theta)$ and in the fibers $p_f(\Theta_f)$ for different values of a_f. In thermodynamic equilibrium, the capillary pressures of the liquid in the inter-fiber and intra-fiber pores are equal. Consequently, the parameter a_f determines the pore-fiber distributions of the liquid in the equilibrium state. For $a_f = 1$, Θ and Θ_f are equal in equilibrium. This case corresponds to the blue, solid, diagonal line in Fig. 3(b), where the non-dimensional equilibrium liquid content in pores $\Theta/\Theta_{\max}$ (solid lines) and fibers $\Theta_f/\Theta_{\mathrm{f,max}}$ (dashed lines) are plotted as a function of the total liquid content $\Theta_{\mathrm{tot}} \equiv \Theta + \Theta_f$ for different values of a_f. For $a_f > 1$, the equilibrium content corresponding to a specific value of the capillary pressure will be higher in the fibers than in the pores. For $a_f \to \infty$ and for increasing total liquid contents Θ_{tot}, the pores will remain essentially empty, while the fibers take up essentially all the liquid until the fiber holding capacity is reached. Only beyond this point, i.e. for $\Theta_{\mathrm{tot}} > \Theta_{\mathrm{f,max}}$, will the pores start to fill, which is illustrated by the green solid and dashed lines in Fig. 3(b).

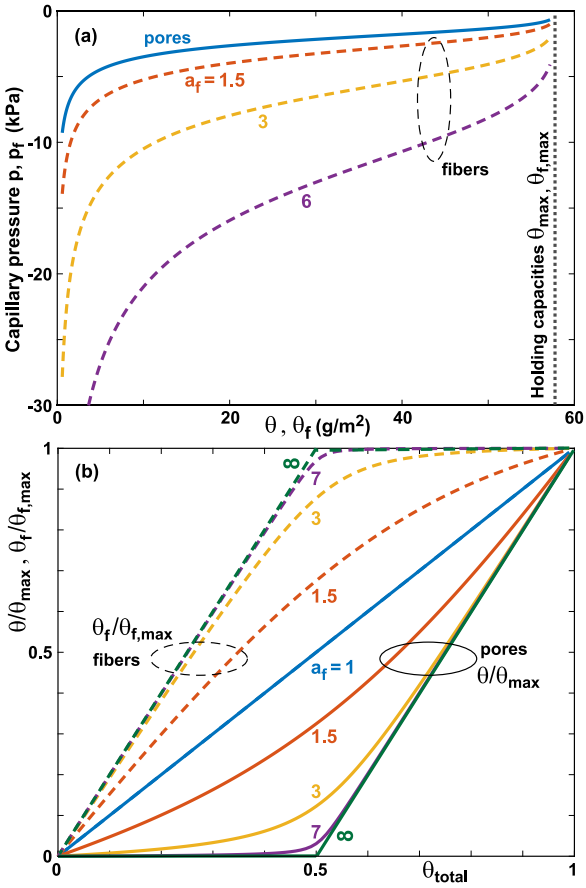

Fig. 3. (a) Capillary pressures in pores p (solid line) and fibers p_f (dashed lines) as functions of corresponding liquid contents Θ and Θ_f for different values of a_f. The vertical dotted line denotes the holding capacities $\Theta_{\max} = \Theta_{\mathrm{f,max}}$. (b) Non-dimensional equilibrium liquid content in pores $\Theta/\Theta_{\max}$ (solid lines) and fibers $\Theta_f/\Theta_{\mathrm{f,max}}$ (dashed lines) as a function of the total liquid content for different values of a_f.

3.2. Pore-fiber transport

In [32], we considered dilute solutions and assumed the pore-fiber transport rate s_{pf} to be proportional to the pressure difference $p_f(\Theta_f) - p(\Theta)$ between pores and fibers [50]. The MW of co-solvents is typically much higher than that of water (see Tab. 1 in the Supplementary Information), which tends to increase viscous friction and reduce s_{pf}. Moreover, in [21] we concluded that the presence of a sufficient quantity of water swells and plasticizes the fiber walls and thereby facilitates the pore-fiber transport of bigger molecules. To account for these effects, we propose to modify s_{pf} as follows

$$s_{pf} = \frac{k_{pf}(MW)}{\mu(MW,c)} f(c)\, g(\Theta_f)\,[p(\Theta) - p_f(\Theta_f)]\,. \tag{18}$$

Here, $k_{pf}(MW)$ is an MW-dependent prefactor. The solution viscosity $\mu(MW,c)$ is strongly concentration dependent, see Fig. 1(a). The function $g(\Theta_f)$ represents the effective permeability of the cellulose fiber walls. We assume it to be given by

$$g(\Theta_f) = (1-\nu)\left(\frac{\Theta_f}{\Theta_{f,\max}}\right)^2 + \nu\,, \tag{19}$$

where $\nu = 0.02$. The function $f(c)$ represents the influence of the co-solvent concentration in the pores. We assume it to be given by:

$$f(c) = \begin{cases} 1 & \text{if } c < c_{\mathrm{crit}} \\ (1-q_r)\exp\left[\frac{1-\frac{c}{c_{\mathrm{crit}}}}{f_q}\right] + q_r & \text{if } c \geq c_{\mathrm{crit}} \end{cases} \tag{20}$$

where $q_r = 0.005$. The parameter c_{crit} denotes the threshold above which the co-solvent concentration starts to affect the pore-fiber transport rate. The parameters f_q and q_r determine the abruptness of the decay of s_{pf} beyond c_{crit} and the baseline rate for $c \gg c_{\mathrm{crit}}$, respectively. Fig. 4 illustrates s_{pf} for $c_{\mathrm{crit}} = 470$ kg/m^3 and three values of f_q.

3.3. Solute and heat transport in paper

We adopt the model and notation of [32] and solve Eqs. (16,23-25) and (27) in [32], rewritten for an axisymmetric system, for the time evolution of the solute concentration in the inter-fiber pores c and the intra-fiber pores c_f (units kg of solute per m^3 of solution), the adsorbed solute concentration C_{ad} as well as the paper temperature T_{paper}. The terms U_{IJ}, j_{IJ} and Φ_s are set to zero. In the following we only point out the modifications and extensions with respect to the model detailed in [22,32].

For axisymmetric flow in the radial direction, only longitudinal dispersion occurs. We use the following expression for the dispersion coefficient D_{eff} [51–53]

$$D_{\mathrm{eff}} = 0.7 D_m(1 + \mathrm{Pe}^{1.2})\,, \tag{21}$$

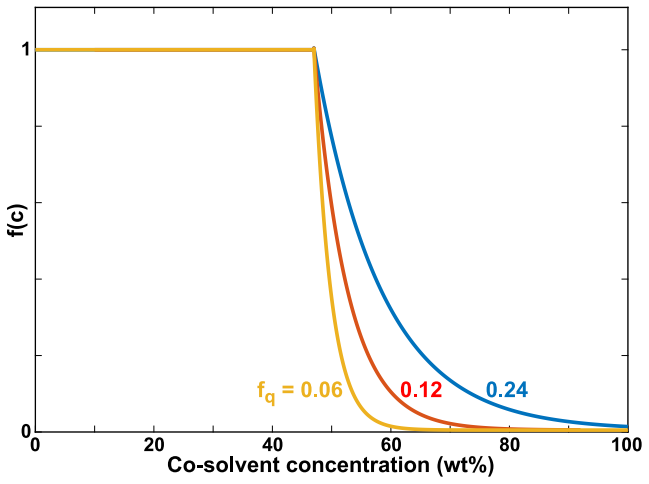

Fig. 4. The function $f(c)$, governing the concentration dependence of the pore-fiber exchange rate s_{pf}, for different values of f_q.

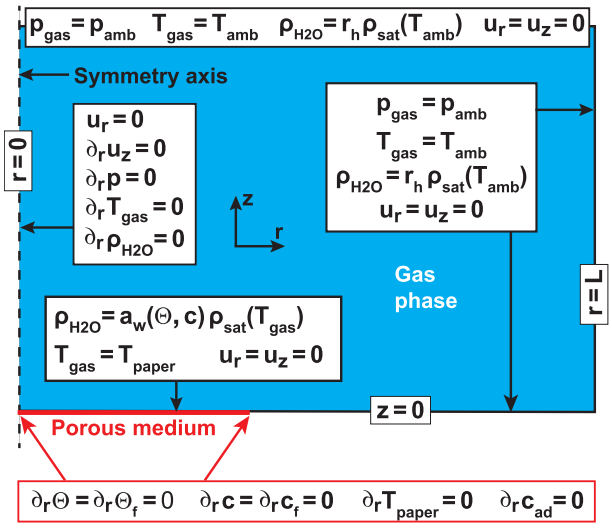

Fig. 5. Boundary conditions for the gas phase domain and the porous medium. The symbol ∂_r is short-hand for $\partial/\partial r$.

where the local Peclet number Pe is given by

$$\mathrm{Pe} \equiv |v| L_{\mathrm{pore}} / D_m \,, \tag{22}$$

where $L_{\mathrm{pore}} = 10\,\mu\mathrm{m}$ is a typical longitudinal lengthscale (cellulose fiber width) and D_m is the molecular diffusion coefficient. Eq. (21) has been obtained for random sphere packings. To the best of our knowledge, experimental or computational studies for fibrous, paper-like materials are not available.

For the transport of co-solvent solutions, adsorption effects are usually weak, because the adsorption capacity is much smaller than the deposited co-solvent content. In contrast, for the transport of dilute solutions, adsorption is a strong effect, contributing to chromatographic retention [5].

3.4. Gas phase transport

We adopt the model of [36], rewritten for an axisymmetric system, and solve for the velocity $\vec{\mathbf{u}} = (u_r, u_z)$ and the temperature T_{gas} of the gas phase, as well as the water vapor mass density $\rho_{\mathrm{H_2O}}$.

3.5. Coupling the paper and gas domains

In contrast to [22,32], the heat exchange with the gas phase via thermal conduction and evaporative cooling is now accurately accounted for by the expression

$$q_{2D} = k_{\mathrm{gas}} \frac{\partial T_{\mathrm{gas}}}{\partial z} + E_{ev} j_{ev} \,, \tag{23}$$

where E_{ev} is the enthalpy of evaporation of water and j_{ev} is the evaporative mass flux. Specifically, the position dependence of the evaporative flux is accurately accounted for by the expression

$$j_{ev} \equiv j_{ev,p} + j_{ev,f} = D_{\mathrm{H_2O}} \frac{\partial \rho_{\mathrm{H_2O}}}{\partial z} \,, \tag{24}$$

where $D_{\mathrm{H_2O}}$ is the diffusion coefficient of water vapor in air. The evaporative flux is split into a contribution from the inter-fiber pores $j_{ev,p}$ and a separate one from the intra-fiber pores $j_{ev,f}$

$$j_{ev,p} = j_{ev} \frac{\Theta}{\Theta + j_f \Theta_f} \,, \tag{25}$$

$$j_{ev,f} = j_{ev} \frac{j_f \Theta_f}{\Theta + j_f \Theta_f} \,. \tag{26}$$

Here, $j_f = 0.2$ is a constant that accounts for the increased mass transfer resistance for evaporation from the fibers, as the water first has to go through the fiber walls. In Eqs. (23), (24) we only consider the gas phase above the paper for simplicity.

The coupling between the paper- and the gas domain is done by assuming continuity of temperature

$$T_{\mathrm{gas}}(r, z = 0, t) = T_{\mathrm{paper}} \,. \tag{27}$$

Moreover, the water vapor density ρ_{H2O} at the paper surface $z = 0$ is determined by the effective sorption isotherm of the porous medium as described in Section 2.1

$$\rho_{\mathrm{H_2O}}(r, z = 0, t) = a_w(\Theta, \Theta_f, c, c_f)\, \rho_{\mathrm{sat}}(T_{\mathrm{gas}}) \,. \tag{28}$$

3.6. Boundary conditions (BCs)

All simulations are conducted assuming axisymmetry, with a gas domain of radius $L = 0.1\,\mathrm{m}$ and height $H = 0.2\,\mathrm{m}$. The thermodynamic variables on the upper and right boundaries of the gas phase domain are assumed to be determined by the ambient conditions (temperature $T_{\mathrm{amb}} = 298\,\mathrm{K}$, relative humidity r_h, atmospheric pressure $p_{\mathrm{amb}} = 1\,\mathrm{bar}$)

$$T_{\mathrm{gas}}(r = L, z) = T_{\mathrm{gas}}(r, z = H) = T_{\mathrm{amb}} \tag{29}$$

$$\rho_{\mathrm{H_2O}}(r = L, z) = \rho_{\mathrm{H_2O}}(r, z = H) = r_h \rho_{\mathrm{sat}}(T_{\mathrm{amb}}) \tag{30}$$

$$p_{\mathrm{gas}}(r = L, z) = p_{\mathrm{gas}}(r, z = H) = p_{\mathrm{amb}} \,. \tag{31}$$

Moreover, we assume the radial and vertical velocity components (u_r, u_z) to be zero there as well as on the lower boundary $z = 0$

$$u_r(r = L, z) = u_r(r, z = H) = u_r(r, z = 0) = 0 \tag{32}$$

$$u_z(r = L, z) = u_z(r, z = H) = u_z(r, z = 0) = 0 \,. \tag{33}$$

The BCs on the left boundary $r = 0$ represent axisymmetry. An overview of all BCs is provided in Fig. 5 for the case where the radial extension of the porous substrate R_p is smaller than L. The BCs for the dynamics inside the porous medium at its perimeter are no-flux conditions, i.e. all radial derivatives vanish at $r = 0$ and $r = R_p$.

We have also considered systems with $R_p = L$ or where a gas phase is present also below the paper substrate. An adapted version of Fig. 5 is presented in the Supplementary Information.

3.7. Initial conditions (ICs)

We do not model the deposition of the liquid. Rather, we assume that the imbibition process is already complete at $t = 0$ and that an

Table 1
Default values of key parameters.

Symbol	Name	Value	Units
a_f	Prefactor in Eq. (17)	3	–
c_0	Initial solute concentration	40	wt%
f_q	Abruptness of decay of s_{pf}	0.012	–
k_{pf}	Pore-fiber exchange rate	$7 \cdot 10^{-9}$	kg/m^2
R_0	Initial wet zone radius	5	mm
ϵ	Transition width	500	μm
Θ_0	Initial liquid pore content	47.5	g/m^2

initial ink distribution with radius $R_0 \leq R_p$ is present in the pores given by

$$\frac{c(r,t=0)}{c_0} = \mathrm{f_{hs}}\left(\frac{R_0 - r}{\epsilon}\right) = \frac{\Theta(r,t=0) - \Theta(\mathrm{amb})}{\Theta_0}\,. \tag{34}$$

Here, c_0 is the initial solute concentration, Θ_0 the initial deposited ink content and $\mathrm{f_{hs}}$ is a smooth Heaviside function with two continuous derivatives

$$\mathrm{f_{hs}}(\tilde{x}) = \begin{cases} 0 & \text{for } \tilde{x} < -1 \\ 1 & \text{for } \tilde{x} > 1 \\ \frac{1}{2} + \frac{15}{16}\tilde{x} - \frac{5}{8}\tilde{x}^3 + \frac{3}{16}\tilde{x}^5 & \text{otherwise}\,. \end{cases} \tag{35}$$

The parameter ϵ denotes the transition width, i.e. a smaller value of ϵ corresponds to a more abrupt transition.

We assume that no solute is present in the fibers initially, i.e. $c_f(t = 0) = 0$, but that the fibers contain the same quantity of water $\Theta_f(\mathrm{amb})$ as dry paper in equilibrium with the ambient atmosphere. Similarly, the same quantity of water $\Theta(\mathrm{amb})$ is contained in the pores at $r > R_0 + \epsilon$ as present in dry paper in equilibrium with the ambient atmosphere. Both $\Theta_f(\mathrm{amb})$ and $\Theta(\mathrm{amb})$ are determined by the effective sorption isotherm of the porous medium and the condition of equal capillary pressure.

We assume there is no initially adsorbed solute

$$C_{\mathrm{ad}}(r,t=0) = 0\,. \tag{36}$$

We initialize the gas phase with zero velocity and constant temperature

$$u_r(t=0) = u_z(t=0) = 0 \tag{37}$$

$$T_{\mathrm{paper}}(t=0) = T_{\mathrm{gas}}(t=0) = T_{\mathrm{amb}}\,. \tag{38}$$

If we would assume the gas phase to have an initially uniform water vapor concentration of $\rho_{\mathrm{H_2O}}(\mathrm{amb}) \equiv r_h \rho_{\mathrm{sat}}(T_{\mathrm{amb}})$, then the initial evaporation rate would be infinite above the wet zone, which is numerically problematic. Therefore, we assume that $\rho_{\mathrm{H_2O}}$ is initialized with an exponentially decaying function above the wet zone

$$\rho_{\mathrm{H_2O}}(t=0) = \rho_{\mathrm{H_2O}}(\mathrm{amb}) + A(r)\exp(-z/d_0).$$

The amplitude $A(r)$ is equal the difference between $\rho_{\mathrm{H_2O}}(\mathrm{amb})$ and Eq. (28); the decay length $d_0 \approx 1$ mm. The influence of this IC disappears typically within a few seconds, which is short compared to the drying time, which is typically 5-10 min.

4. Numerical results

We performed a systematic parameter study using the material parameters of TEG. Unless mentioned otherwise the default values of important parameters are those listed in Table 1. A complete list of all symbols and parameter values is provided at the end of the Supplementary Information.

4.1. Model validation

For the purpose of validation we considered the drying dynamics of a papersheet after deposition of a droplet of pure water, for which quantitative experimental data were available in [21]. Details are provided in the Supplementary Information.

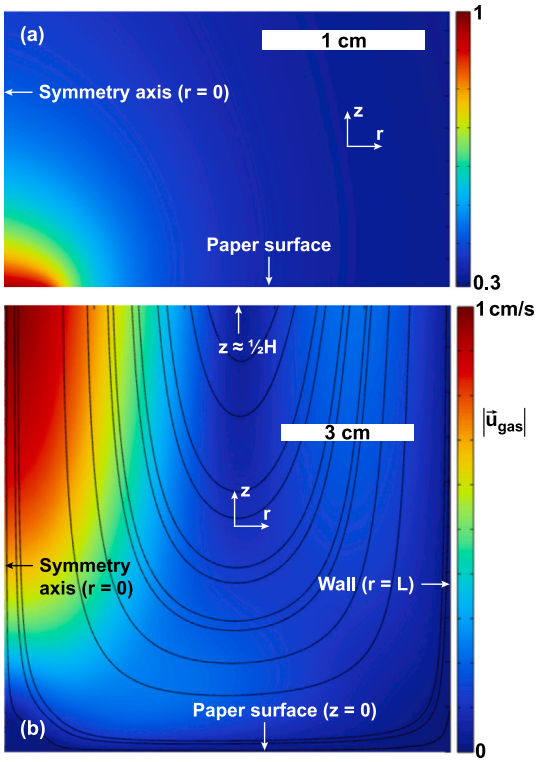

Fig. 6. Pseudo-color plots of (a) the normalized water vapor density $\rho_{\mathrm{H_2O}}/\rho_{\mathrm{sat}}(T_{\mathrm{amb}})$ and (b) the velocity distribution $|\vec{\mathbf{u}}_{\mathrm{gas}}|$ in the gas phase at $t = 120$ s after deposition of a droplet of pure water ($V = 5$ μl). The solid lines in (b) represent streamlines.

4.2. Gas phase dynamics

Fig. 6(a) shows the normalized water vapor density $\rho_{\mathrm{H_2O}}/\rho_{\mathrm{sat}}(T_{\mathrm{amb}})$ above a paper substrate at $t = 120$ s after deposition of pure water, for an ambient relative humidity $r_h = 29.7\%$. Fig. 6(b) shows the magnitude of gas velocity distribution and selected streamlines.

The gas density ρ_{gas} is affected by both temperature and humidity variations, which induce buoyancy-driven convection. Where water evaporates from paper, the local humidity in the adjacent gas increases, but the temperature drops due to evaporative cooling. As ρ_{gas} decreases with increasing humidity but increases with decreasing temperature, these two mechanisms are antagonistic. Temperature variations are on order of a few K corresponding to a relative density change $\Delta\rho_{\mathrm{gas}}/\rho_{\mathrm{gas}} \approx 1\%$. Variations in relative humidity are on order of 60%, corresponding to $\Delta\rho_{\mathrm{gas}}/\rho_{\mathrm{gas}} \approx 2\%$. Therefore, humidity variations tend to govern the large scale convection pattern.

In Fig. 6(b), a plume with upwards flow is observed above the wet zone. Its maximum velocity is about $|\vec{\mathbf{u}}|_{\max} \approx 1$ cm/s. This corresponds to a Reynolds number $\mathrm{Re}_L = \rho_{\mathrm{gas}} u_{\max} L/\mu_{\mathrm{gas}} \approx 60$, which implies that inertial effects are important, but that the flow is laminar. Here $L = 10$ cm is the width of the computational domain. The value of the Peclet number is $\mathrm{Pe}_R = u_{\max} R_0/D_{\mathrm{H2O}} = 2$, which indicates that the water vapor transport is essentially diffusion dominated, but that convection effects cannot be neglected. The same conclusion holds for heat transfer in the gas phase, as the Lewis number of air $\mathrm{Le} = \alpha_{\mathrm{air}}/D_{\mathrm{H2O}}$ is close to 1. Here, α_{air} is the thermal diffusivity of air.

4.3. Co-solvent transport

Fig. 7(a) shows the distributions of the co-solvent content in the inter-fiber pores $\Theta_{\mathrm{cs}} \equiv c\Theta/\rho_{\mathrm{liq}}$ for different droplet volumes V, at $t = 160$ s. At this point in time, the co-solvent pore-fiber distributions are already quasi-steady. The vertical dashed lines denote the initial

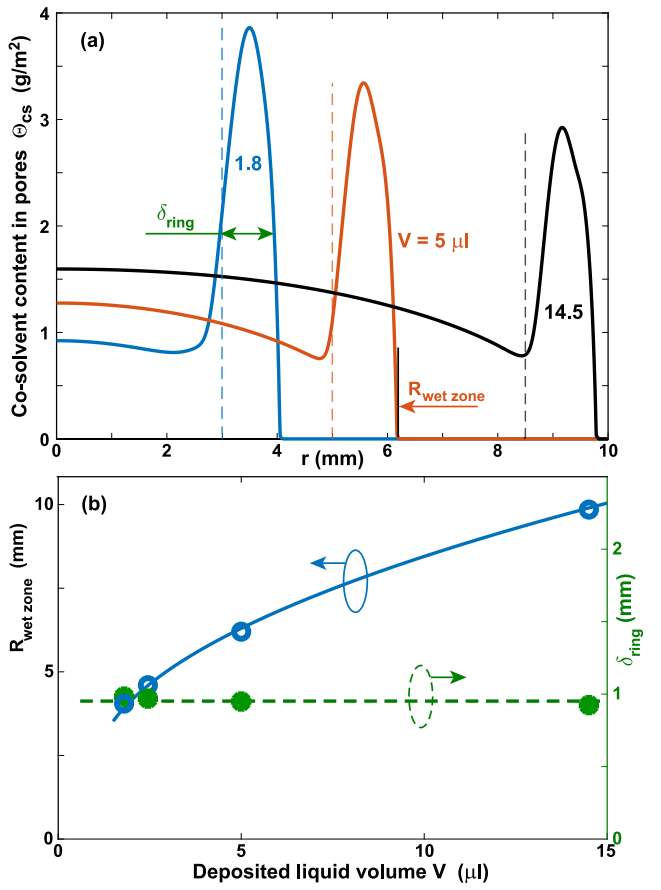

Fig. 7. (a) Co-solvent content in inter-fiber pores Θ_{cs} for different deposited liquid volumes V at $t = 160$ s. (b) Radius of the wet zone $R_{wet\ zone}$ (open circles and blue solid line) and width of the ring stain δ_{ring} (green circles and green dashed line) as a function of V.

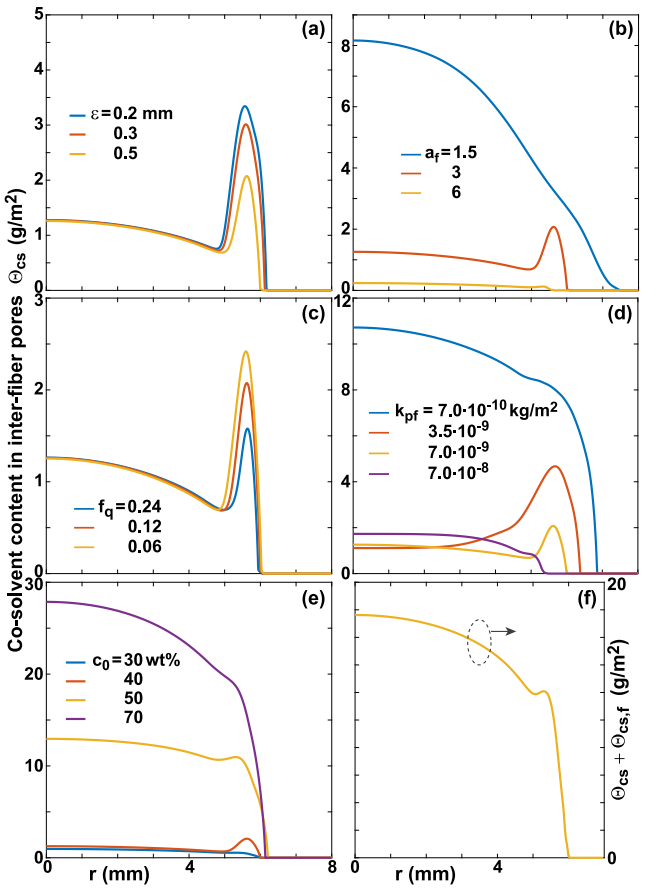

Fig. 8. Co-solvent distribution in inter-fiber pores Θ_{cs} for different values of (a) ϵ, (b) a_f, (c) f_q, (d) k_{pf} and (e) c_0, all at $t = 160$ s. (f) Total co-solvent content $\Theta_{cs} + \Theta_{cs,f}$ in pores and fibers for the default parameter values in Table 1.

radii of the wet zones. Fig. 7(b) shows the radius of the wet zone $R_{wet\ zone}$ and the width of the ring stain δ_{ring} (defined as the full width at half maximum) as a function of V. The blue solid line corresponds to a fit function

$$R_{wet\ zone} = A + B(V - V_0)^{1/2} \tag{39}$$

with fitparameters A, B and V_0. The exponent 1/2 follows from mass conservation for drop volumes sufficiently large to completely penetrate the substrate thickness t_p. The green dashed line in Fig. 7(b) represents a constant value of δ_{ring}. Both curves are in good qualitative agreement with Fig. 5(b) in [21]. However, in the experiments in [21], the amplitude of the ring stain decreases with decreasing volume, whereas in Fig. 7(a) it increases. In the three curves in Fig. 7(a), the value of ϵ is identical. It is conceivable that in the experiments ϵ was not independent of V.

Fig. 8(a) shows the co-solvent distribution in the inter-fiber pores for different values of the transition width ϵ at $t = 160$ s. The amplitude of the ring stain decreases with increasing ϵ. The reason is that the local water evaporation rate is higher for sharper transitions. As a result, the concentration c exceeds the threshold c_{crit} sooner and thus more co-solvent is trapped in the pores. Since a sharper initial distribution causes a stronger Darcy flow, the radius of the wet zone increases slightly more for smaller value of ϵ.

Fig. 8(b) shows co-solvent content in the pores for different values of a_f. Larger values of a_f reduce the quasi-steady co-solvent content in the inter-fiber pores. There are two effects at play. Firstly, a_f increases the pressure differential in Eq. (18), i.e. the driving force for pore-fiber transport. A larger value of a_f thus reduces the timescale for pore-fiber equilibration and decreases the co-solvent content in the pores. A second factor is the higher equilibrium co-solvent content in the inter-fiber pores for lower values of a_f, as illustrated by Fig. 3. This will lead to considerable co-solvent contents in the inter-fiber pores — even if pore-fiber equilibrium is reached.

As shown in Fig. 8(b), the radius of the wet zone increases for smaller value of a_f. The reason is that smaller value of a_f implies slower pore-fiber transport. Consequently, Darcy flow induced spreading occurs at a higher rate, primarily because the permeability K is a nonlinear function of Θ [22].

Fig. 8(c) shows the co-solvent content in the inter-fiber pores after a quasi-steady state is obtained. The maximum amplitude of the co-solvent content in the ring-stain increases for smaller f_q. This is because a faster decay of the function $f(c)$ reduces the pore-fiber transport rate sooner, and thus leaving more co-solvent trapped in the inter-fiber pores.

Fig. 8(d) shows co-solvent distribution for different k_{pf} at $t = 160$ s. For smaller k_{pf}, liquid transport between pores and fibers is slower, whereas evaporation is unchanged. As a result, more co-solvent will be trapped in the pores, especially near the perimeter of the wet zone, where evaporation is highest. The larger amount of liquid in the fibers, the smaller will be the wet-zone diameter, because liquid is assumed immobile in the fibers according to Eq. (16). For $k_{pf} = 7 \cdot 10^{-9}$ and $3.5 \cdot 10^{-9}$ kg/m^2, a pronounce ring stain is observed. Its amplitude and width are larger for the smaller value of k_{pf}. This is in good qualitative agreement with the experimental data for TEG and PEG-6 in Fig. 3(g) of [21].

Fig. 8(e) shows the co-solvent distribution in the inter-fiber pores for different initial concentrations c_0 at $t = 160\,\mathrm{s}$. For larger values of c_0, more co-solvent is retained in the inter-fiber pores. The reason is that the threshold c_{crit} is exceeded from the outset for $c_0 \geq 50$ wt%.

In Fig. 8(f) we plotted the total co-solvent content in pores and fibers $\Theta_{\mathrm{cs}} + \Theta_{\mathrm{cs,f}}$ for the default parameter values in Table 1. It is clearly observed that no pronounced peak is visible at the perimeter of the wet zone, in contrast to the peaks in the inter-fiber pore content observed in e.g. Figs. 7(a) or 8(a,b). Rather, the overall distribution resembles that of an initially uniform distribution that has undergone some radial spreading in a regular porous medium with impermeable solid phase. Only a small shoulder is present at $r \approx R$. The shape qualitatively agrees with the experimental data for the capacitance increment in Fig. 6(b) of [21], which is sensitive to the total liquid content.

5. Discussion

5.1. Evaporative flux near wet zone boundaries

The coffee stain effect for sessile droplets on impermeable surfaces is enhanced by the strong non-uniformity of the evaporative flux, which exhibits a singularity of the form

$$j_{\mathrm{ev}}(r) \sim (R_{\mathrm{drop}} - r)^{-1/2} \tag{40}$$

for the case of small contact angles and slow, diffusion-limited evaporation [1]. Here, R_{drop} is the footprint radius of the droplet, which is assumed to have a spherical-cap shape. The singularity arises from the abrupt change in BC for solvent vapor transport from a constant vapor pressure at the liquid–air interface to a no-flux condition beyond the droplet footprint. Although unphysical, the singularity is integrable, i.e. the overall mass flux remains finite.

For slow, diffusion-limited evaporation, the time-derivative in Eq. (12) of [36] can be neglected [54]. Moreover, near the surface at $z = 0$, the air velocity is small owing to the no-slip BC. Therefore, the convective term in Eq. (12) of [36] can be neglected as well, leading to the Laplace equation

$$\Delta \rho_{\mathrm{H_2O}} = 0\,. \tag{41}$$

After droplet deposition on a porous medium, there is no abrupt change in the *type* of BC, which for volatile droplets on impermeable substrates changes from Dirichlet- to Neumann type. However, there can still occur an abrupt change in the *magnitude* of the vapor pressure according to Eq. (8), which is a Dirichlet BC for Eq. (41). In the next paragraph, we show that this also leads to a singularity in the evaporative flux.

Using an integral transform approach [55], the following analytical solution of the Laplace equation $\Delta c = 0$ for a semi-infinite 2D domain with piece-wise constant but discontinuous Dirichlet BCs

$$c(x < 0, z = 0) = c_1 \quad \text{and} \quad c(x > 0, z = 0) = c_2 \tag{42}$$

can be derived

$$c(x, z) = c_2 + (c_1 - c_2)\left[\frac{1}{2} - \frac{1}{\pi}\arctan\left(\frac{x}{z}\right)\right]. \tag{43}$$

Thus, the evaporative flux $j_{\mathrm{ev}}(x)$ is proportional to

$$\frac{\partial c}{\partial z}(x, z = 0) \;=\; \frac{c_1 - c_2}{\pi}\,\frac{1}{x}\,. \tag{44}$$

Fig. 9 compares numerical solutions for the boundary flux $\left|\frac{\partial c}{\partial z}\right|$ as a function of $|x|$ with Eq. (44). The latter exhibits an unphysical, *non-integrable* singularity due to the boundary discontinuity. However, this does not pose an essential problem in practice, because in a homogeneous porous medium, a discontinuous liquid distribution would induce a singular Darcy flow, thus removing the discontinuity in an instant. In contrast, the (integrable) singular evaporative flux near the contact line of a sessile droplet *persists* in time, because the discontinuity of the liquid distribution remains present until the contact line depins or the evaporation is complete.

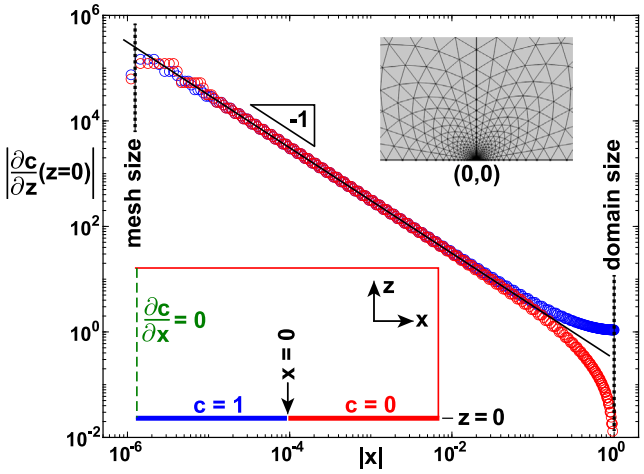

Fig. 9. Boundary flux $\left|\frac{\partial c}{\partial z}(z = 0)\right|$ as a function of $|x|$ corresponding to the solution of the Laplace equation on a 2D halfspace with discontinuous Dirichlet boundary conditions according to Eqs. (42). The symbols represent a numerical finite-element solution, the black solid line corresponds to Eq. (44). The dotted vertical lines indicate the mesh size in the vicinity of the discontinuity at $x = 0$ and the halfwidth of the simulation domain, respectively. The insets illustrate the BCs and the non-uniform finite-element mesh around the origin.

5.2. Coffee stain formation in thin porous media

After deposition of a droplet on a thin porous medium, the non-uniform liquid distribution sets up a non-uniform evaporative flux and induces a Darcy flux directed radially outward [see e.g. Fig. 5(b) in the Supplementary Information]. Therefore, in principle, a coffee-stain-like effect can also occur for solutions in porous media. However, for dilute solutions, chromatographic retention [5] often depletes the solute near the perimeter of the wet zone. Moreover, the Darcy flow is usually *decelerating*, as the gradients in the liquid content become shallower in time [see e.g. Fig. 5(b) in the Supplementary Information], in contrast to the flow in a sessile volatile droplet, which *accelerates* in time [1].

Exceptions of practical relevance exist for wet zones that extend to the perimeter of a paper substrate or a hydrophobic barrier. In these cases, the liquid distribution exhibits a *persistent* discontinuity at the edges of the porous sheet or the wettable region. The flux singularity is then expected to be integrable with exponent $-1/2$, due to the no-flux condition relevant beyond the perimeter of the paper sheet or on top of the hydrophobic barrier [9–15].

Fig. 10(a) shows numerical simulations of the solute distribution Θ_{cs} in the inter-fiber pores for circular paper substrates with finite radius R_p that were initially homogeneously wet. The ICs used deviate slightly from those in Section 3.7 and Table 1 in that

$$\Theta_0 = 57\,\mathrm{g/m^2} = \Theta_{f,0}\,. \tag{45}$$

A pronounced peak in the solute content is observed at the substrate edge at $r = R_p = 5$ mm for sufficiently small values of D_m. Fig. 10(b) presents a zoom of (a) near $r = R_p$. Fig. 10(c) shows the width of the solute peak w as a function of D_m. The width is defined as the half-width-at-half-maximum (HWHM) between the minimum of Θ_{cs} at $r = 0$ and its maximum at $r = R_p$, as indicated by the red arrow in Fig. 10(a). The red solid line in Fig. 10(c) is a power law fit $w \sim D_m^{0.55}$.

Nilghaz et al. presented experiments of the evaporation of dye solutions in paper, and observed pronounced coffee-stains at hydrophobic barriers and edges of finite-area paper substrates (see Figs. 7 and 9(b) in [9]), whereas no coffee stains were observed for droplets deposited on large-area substrates. Our simulations in Fig. 10 qualitatively reproduce their results. Fig. 10(c) suggests that an estimate for the solute diffusion coefficient can be obtained from the width of the coffee stain.

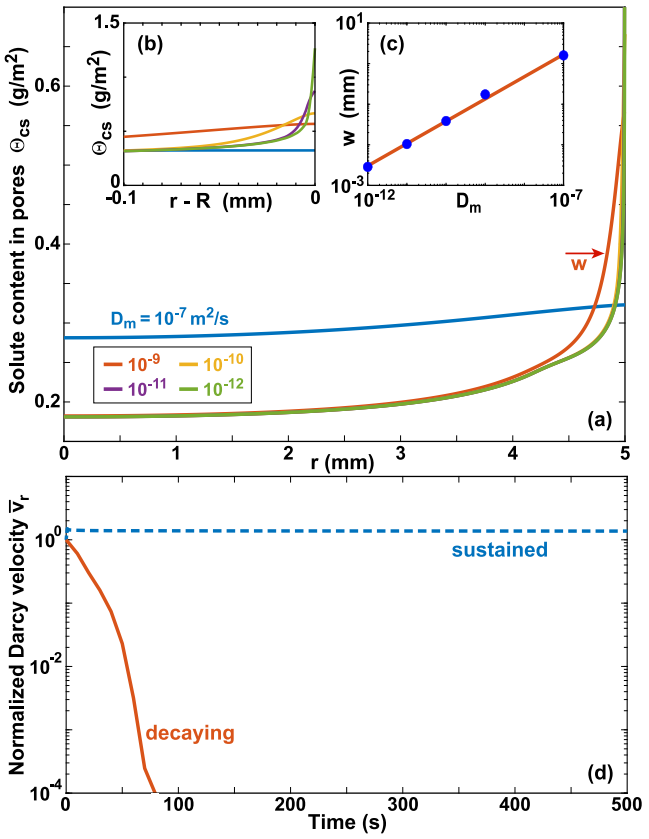

Fig. 10. (a) Solute distribution in the inter-fiber pores Θ_{cs} for different values of D_m, for homogeneously wetted substrates with limited area. (b) Zoom of (a) near the edge of the substrate. (c) Halfwidth w of the solute peak near the substrate edge as a function of D_m. (d) Normalized Darcy velocity $\bar{v}(r^*, t)$ at fixed radial positions. The red solid line represents the red curve in Fig. 7 at $r^* = r/R_0 = 1$. The blue dashed line corresponds to the curves in (a) at $r^* = r/R_0 = 0.9$.

5.3. Difference between coffee stains & solute rings

The distinguishing feature between the co-solvent rings observed in Ref. [21] and e.g. Fig. 8(d) and the *coffee-stains* in Ref. [9] and Fig. 10, is that the latter involve *sustained* solute transport towards the edge. This is illustrated in Fig. 10(d), where the normalized Darcy velocity

$$\bar{v}(r^*, t) \equiv \frac{v(r^*, t)}{v(r^*, t = 0)} \tag{46}$$

is plotted at fixed radial positions r^*. The solid line represents the simulation shown as the red curve in Fig. 7 at $r^* = r/R_0 = 1$. The dashed line corresponds to the curves in Fig. 10(a) at $r^* = r/R_0 = 0.9$. While the velocity decays to 10% of its initial value within approximately 40 s for the red curve, it remains essentially constant for the blue one, during the time interval shown. Moreover, while the co-solvent content in the ring-stains observed in e.g. Fig. 7 is lower than the initial co-solvent content $c_0\Theta_0$ in the inter-fiber pores, the solute content in the coffee-stains in Fig. 10(a,b) is *higher* than the initial value for $D_m \leq 10^{-10}$ m²/s.

5.4. Pore-fiber transport — effect of solute concentration and molecular weight

The selected value of $c_{crit} = 470\,\mathrm{kg/m^3}$ is motivated by the experiments in [21], where it was observed that the residual co-solvent content left in the pores of a paper substrate after deposition and evaporation of an aqueous TEG solution droplet noticeably increased beyond an initial concentration c_0 of approximately 50 wt%. Moreover, it was reported in Ref. [56] that the persistent expansion strain after deposition and evaporation of various aqueous co-solvent solutions monotonically increased for low co-solvent concentrations up to a critical value between 40 and 60 wt%, beyond which it monotonically decreased. This critical value did not seem to depend strongly on the chemical composition nor the MW of the co-solvents considered in Refs. [21,56]. The co-solvent MW therefore appears to primarily affect the values of k_{pf} and possibly also of f_q and q_r, but not so much c_{crit}.

Peppas and Reinhart studied solute transport through swollen polymer membranes [57]. They proposed a linear correlation between the logarithm of the membrane permeability for the solute and the square of the solute molecular radius r_s^2. For solutes of low MW, r_s is expected to scale as $(MW)^{1/3}$. Yasuda et al. [58] and Sato & Kim [59] reported experimental data consistent with this prediction.

Tokita [60] studied the diffusion of probe molecules in cross-linked polyacrylamide gel and observed a good correlation between the gel diffusion coefficient of the solutes and

$$D/D_0 = \exp(-u), \quad \text{where} \quad u \sim (MW)^{1/3} C_{tot}^{-3/4},$$

D_0 is the diffusion coefficient in pure solvent and C_{tot} is the mass density of the gel (not including the solvent) in kg/m³. This result is similar to the relation

$$D \sim \exp(-\kappa r_s) \tag{47}$$

proposed by Ogston et al. [61] and Cukier [62], who studied the diffusion of Brownian spheres in semidilute polymer solutions theoretically. It is consistent with the experimental results of Colton et al. [63] for probe diffusion in cellulosic membranes and of Langevin & Rondelez [64] for colloid transport through semidilute polymer solutions.

In contrast, Brown and Johnsen [65], who studied the MW dependence of the effective diffusion coefficient for low MW solutes through polyacrylamide gels, found a correlation

$$D \sim \begin{cases} (MW)^{-0.55} & \text{for } MW \lesssim 200 \\ (MW)^{-0.30} & \text{for } MW \gtrsim 200\,. \end{cases} \tag{48}$$

Similarly, Nishioka et al. [66], who studied the permeability P of cellulose based membranes, found that

$$P \sim \begin{cases} (MW)^{-1} & \text{for } MW \lesssim 800 \\ (MW)^{-0.33} & \text{for } MW \gtrsim 800\,. \end{cases} \tag{49}$$

Pluen et al. [67] found $D \sim r_s^{-1.15}$ for an agarose gel and $r_s \lesssim 15$ nm.

The above experimental and theoretical results indicate that the pore-fiber transport rate is strongly dependent on MW. According to Eq. (18), the MW-dependent terms in the pore-fiber transport rate s_{pf} are given by k_{pf}/μ, i.e. both k_{pf} and the solution viscosity μ can contribute to the MW dependence of s_{pf}. For non-dilute, aqueous solutions of poly(ethylene glycols), the scaling of μ with MW is well represented by a powerlaw relation

$$\mu \sim (MW)^{\beta}$$

with exponent $0.75 < \beta < 1$, at least up to MW = 300 (see Fig. 3 in the Supplementary Information).

In Fig. 11(a) experimental data for the differential light transmittance $\Delta I/I_0$ are shown, which are taken from Fig. 3(g) in [21]. The three curves represent aqueous solutions of ethylene glycol (EG), TEG and hexa(ethylene glycol) (PEG6). The relation between $\Delta I/I_0$ and Θ is approximately linear for sufficiently large Θ, but non-linear for small Θ [21]. In the corresponding numerical simulations shown in Fig. 11(b), we assumed a constant value of $k_{pf} = 2.4 \cdot 10^{-9}\,\mathrm{kg/m^2}$ for the different co-solvents EG, TEG and PEG6, i.e. that only the viscosity contributes to the MW dependence of s_{pf}. The simulations resemble the experimental curves qualitatively well as for the ratio of the peak heights for TEG and PEG-6. Moreover, the width of the peaks increases with increasing MW in a comparable fashion in both Figs. 11(a) and (b). In Fig. 11(c) we plotted the peak values of co-solvent pore content $\max(\Theta_{cs})$ as a function of co-solvent MW. The solid line represents a linear relation, in excellent qualitative agreement with Fig. 3(h) in [21].

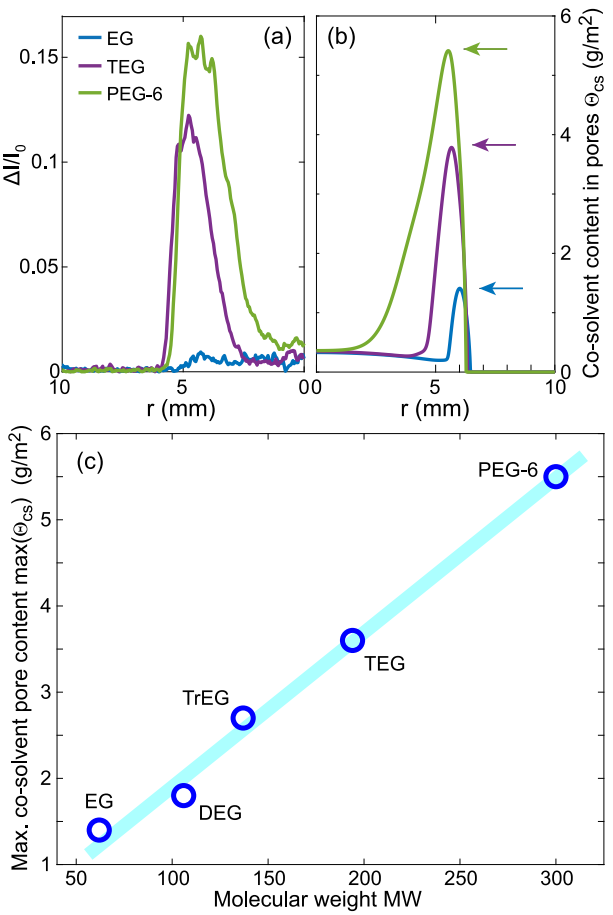

Fig. 11. (a) Experimental data for differential light transmittance $\Delta I/I_0$ after deposition and drying of aqueous EG, TEG and PEG6 solution droplets ($c_0 = 40$ wt%) in paper, taken from Fig. 3(g) in [21]. (b) Numerical simulations of the residual co-solvent content in the pores after deposition and drying of aqueous EG, TEG and PEG6 solution droplets. Here, we have assumed $a_f = 4.5$, $k_{pf} = 2.4 \cdot 10^{-9}$ kg/m^2, $\epsilon = 500\,\mu$m. (c) Peak values of co-solvent pore content as indicated by the horizontal arrows in (b) as a function of co-solvent MW. The solid line is a guide to the eye.

5.5. Rehydration

It was found in [21] that the deposition of pure water on regions where co-solvent is temporarily 'trapped' in the pores greatly facilitates pore-fiber transport. Fig. 12(a) shows an optical transmission image of a paper samples after deposition and drying of a 50 wt% TEG droplet. The gray area with increased transmission is due to residual co-solvent residing in the pores. Fig. 12(b) shows the same sample after deposition and evaporation of two small water droplets in the center. The black 'hole' in the middle exhibits the same transmission as the dry paper in the periphery and arises a consequence of the completed, solvent-assisted pore-fiber transport of TEG [21].

We reproduce this process numerically by application of the following ICs:

$$\Theta(t=0) = \Theta_{\text{out}} + (\Theta_{\text{in}} - \Theta_{\text{out}})\, \text{f}_{\text{hs}}\left(\frac{R_w - r}{\epsilon}\right) \tag{50}$$

$$c(t=0) = c_0 \frac{\Theta_{\text{out}}}{\Theta(t=0)}, \tag{51}$$

$$c_f(t=0) = 0\,. \tag{52}$$

Here, $\Theta_{\text{out}} = 0.2\Theta_{\max}$ denotes the temporarily trapped co-solvent content in the pores and $\Theta_{\text{in}} = 0.7\Theta_{\max}$ the increased liquid content due to deposition of the rehydrating water distribution with radius $R_w = 2$ mm and abruptness parameter $\epsilon = 0.5$ mm. The initial co-solvent content in the pores $\Theta_{\text{cs}}(t=0)$ is assumed independent of r. Thus, the co-solvent concentration c satisfies Eq. (51). Eq. (52) expresses that no co-solvent is initially present in the fibers.

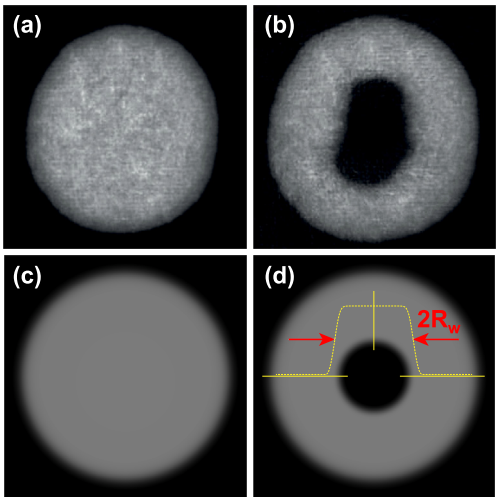

Fig. 12. (a,b) Optical transmission images of paper (a) 30 min. after deposition of a 50 wt% TEG droplet ($V = 5\,\mu$l), and (b) after deposition and subsequent evaporation of two water droplets ($V = 1\,\mu$l) in its center [21]. (c,d) Corresponding numerical simulations with grayscale representing the co-solvent content in the pores. Image widths 12 mm. The dashed line in (d) indicates the initial distribution of the added water.

Figs. 12(c,d) show the initial and the final co-solvent distribution in the pores, after the rehydrating water has evaporated. The similarity with Fig. 12(a,b) is striking.

5.6. Solutocapillary effects

Solutocapillary effects due to the concentration dependence of surface tension $\gamma(c)$ are relatively weak in the co-solvent ring formation process, because they are essentially quenched by the strong increase of viscosity $\mu(c)$. This is in stark contrast to dilute surfactant solutions [32], where $\gamma(c)$ strongly influences the ink redistribution and $\mu(c)$ does not change as much.

5.7. Material parameters and closure relations

Models for the transport of liquids and solutions in unsaturated porous media based on the Richards equation are conceptually attractive, because they explicitly take the governing physical processes and corresponding state variables into account. Their main disadvantage is that they require a large number of material parameters and closure relations that are often not available from published experimental data. The fact that the detailed composition and properties of commercial paper grades are usually maintained confidential adds to the problem. Therefore, we resolved to using empirical relations, some of which are well-established in literature and some were newly introduced. Examples include the

1. Van Genuchten relations for the capillary pressures p and p_f in Eqs. (14), (17) and the effective permeability as a function of liquid content.
2. Dispersion relation according to Eq. (21).
3. Langmuir solute adsorption dynamics according to Eq. (27) in [32].
4. Water activity: we assume that Eqs. (3), (7), which are accurate for the two-component systems water/paper and water/co-solvent, also hold for the three-component system water/paper/co-solvent.

5. Pore-fiber exchange rate, Eqs. (18)–(20).
6. Evaporation rates in Eqs. (25), (26).

To improve the accuracy of our model, the parameters relevant to items 1–4 in the above list need to be calibrated against dedicated experiments. The last two items would benefit from pore-resolved models and experiments [68–72] and dedicated single-fiber experiments [73–76].

6. Summary and conclusions

We have developed a numerical model for the transport and drying of solutions with volatile solvents in thin porous media. Our model explicitly includes the gas phase above the porous medium and therefore yields realistic evaporative flux distributions for the case of diffusion-limited evaporation. This is crucial for studying the coffee-stain effect in porous media, which is well reproduced by our model. In the case of sessile droplets on impermeable surfaces, the evaporative flux exhibits a singularity at the contact line with an exponent of $-1/2$. In contrast, we found a flux singularity with exponent -1 for abrupt changes in liquid content in a homogeneous thin porous medium. In experiments, coffee-stains are primarily observed at the perimeter of media of finite dimensions or of moisture distributions confined by hydrophobic barriers. In these cases, the corresponding flux singularity exponent is $-1/2$.

We also investigated the occurrence of solute rings after deposition of concentrated aqueous solutions of co-solvents such as glycerol. Although their appearance resembles coffee-stains, their origin is different and associated with delayed pore-fiber transport in media with permeable fibers. We introduced an empirical relation for the concentration- and molecular-weight dependence of the pore-fiber transport rate of co-solvents. Our results indicate that the main contribution to the molecular-weight dependence stems from the solution viscosity.

Our model reproduces the available experimental data qualitatively well. It can therefore aid in the further development of inkjet printing technology, where transport and distribution of e.g. colorants needs to be tightly controlled to safeguard the color intensity and uniformity of printed patterns. Moreover, it can assist in the design of sensor devices based on paper microfluidics that e.g. capitalize on the concentration enhancement of solutes due to the coffee-stain effect.

CRediT authorship contribution statement

S. Wang: Investigation, Software, Writing – original draft. **A.A. Darhuber:** Conceptualization, Investigation, Supervision, Writing – review & editing.

Declaration of competing interest

The authors declare that they have no known competing financial interests or personal relationships that could have appeared to influence the work reported in this paper.

Data availability

Data will be made available on request.

Acknowledgments

This work is part of an Industrial Partnership Programme (i43-FIP) of the Foundation for Fundamental Research on Matter (FOM), which is part of the Netherlands Organization for Scientific Research (NWO). This research programme is co-financed by Canon Production Printing, University of Twente, Eindhoven University of Technology, and the "Topconsortia voor Kennis en lnnovatie (TKl)" allowance from the Ministry of Economic Affairs. The authors thank Nicolae Tomozeiu of Canon Production Printing for the fruitful cooperation.

Appendix A. Supplementary data

Supplementary material related to this article can be found online at https://doi.org/10.1016/j.colsurfa.2023.132839.

References

[1] R.D. Deegan, O. Bakajin, T.F. Dupont, G. Huber, S.R. Nagel, T.A. Witten, Capillary flow as the cause of ring stains from dried liquid drops, Nature 389 (1997) 827–829.
[2] R. Dou, B. Derby, Formation of coffee stains on porous surfaces, Langmuir 28 (2012) 5331–5338.
[3] Z. Huang, A. Nagpal, S. Siddhanta, I. Barman, Leveraging coffee-ring effect on plasmonic paper substrate for sensitive analyte detection using Raman spectroscopy, J. Raman Spectrosc. 49 (2018) 1552–1558.
[4] W. Li, W. Ji, D. Lan, K. Wu, Y. Wang, Absorption induced ordered ring and inner network structures on a nanoporous substrate, RSC Adv. 10 (2020) 22595–22599.
[5] G. Venditti, V. Murali, A.A. Darhuber, Chromatographic effects in inkjet printing, Langmuir 37 (2021) 11726–11736.
[6] D. Zhang, B. Ma, L. Tang, H. Liu, Toward quantitative chemical analysis using a ruler on paper: An approach to transduce color to length based on coffee-ring effect, Anal. Chem. 90 (2018) 1482–1486.
[7] D. Zhang, B. Gao, Y. Chen, H. Liu, Converting colour to length based on the coffee-ring effect for quantitative immunoassays using a ruler as readout, Lab Chip 18 (2018) 271–275.
[8] R. Ghosh, V. Vaishampayan, A. Mahapatra, R. Malhotra, S. Balasubramanian, A. Kapoor, Enhancement of limit of detection by inducing coffee-ring effect in water quality monitoring microfluidic paper-based devices, Desalination Water Treat. 156 (2019) 316–322.
[9] A. Nilghaz, L. Zhang, W. Shen, Coffee stains on paper, Chem. Eng. Sci. 129 (2015) 34–41.
[10] E. Trofimchuk, A. Nilghaz, S. Sun, X. Lu, Determination of norfloxacin residues in foods by exploiting the coffee-ring effect and paper-based microfluidics device coupling with smartphone-based detection, J. Food Sci. 85 (2020) 736–743.
[11] E. Trofimchuk, Y. Hu, A. Nilghaz, M.Z. Hua, S. Sun, X. Lu, Development of paper-based microfluidic device for the determination of nitrite in meat, Food Chem. 316 (2020) 126396.
[12] M.L. Choobbari, M.B. Rad, A. Jahanshahi, H. Ghourchian, A sample volume independent paper microfluidic device for quantifying glucose in real human plasma, Microfluid. Nanofluid. 24 (2020) 74.
[13] R.H. Müller, D.L. Clegg, Automatic paper chromatography, Anal. Chem. 21 (1949) 1123–1125.
[14] E. Carrilho, A.W. Martinez, G.M. Whitesides, Understanding wax printing: A simple micropatterning process for paper-based microfluidics, Anal. Chem. 81 (2009) 7091–7095.
[15] J. Olkkonen, K. Lehtinen, T. Erho, Flexographically printed fluidic structures in paper, Anal. Chem. 82 (2010) 10246–10250.
[16] C. Schmid, in: S. Magdassi (Ed.), Formulation and Properties of Waterborne Inkjet Inks, World Scientific, Singapore, 2010, Ch. 7.
[17] G.W. Byers, R. Anderson, M.L. Choy, Cosolvents in printing fluids, US Patent 2006/0065155A1.
[18] K.M. Kosydar, R.P. Szajewski, Inkjet printer with inks containing polyoxygenated-polyols, US Patent 8, 936, 357 B2.
[19] T. Inoue, T. Ohashi, Y. Fujimoto, Process for producing oriented polymeric film, US Patent US5207824A.
[20] R. Mittal, R.S. Shaffer, P. Chien, B.L. Piekarski, Methods and systems for providing enhanced user interfaces for generating symbolic media, US Patent US8613509B2.
[21] M.G. Wijburg, S. Wang, A.A. Darhuber, Transport and evaporation of aqueous co-solvent solutions in thin porous media, Colloids Surf. A 656 (2023) 130268.
[22] V. Murali, G. Venditti, J.C. Zeegers, A.A. Darhuber, Inkjet deposition of lines onto thin moving porous media - experiments and simulations, Int. J. Heat Mass Transfer 176 (2021) 121466.
[23] M. Ek, G. Gellerstedt, G. Henriksson (Eds.), Paper Products Physics and Technology, de Gruyter, 2009.
[24] D.W. Lyons, C.T. Vollers, A.M. ElNashar, Contact drying of a sheet of moist fibrous material, J. Eng. Ind. 102 (1980) 8–12.
[25] S. Ramaswamy, R.A. Holm, Analysis of heat and mass transfer during drying of paper/board, Dry. Technol. 17 (1999) 50–72.
[26] S. Reardon, M. Davis, P. Doe, Computational modeling of paper drying machines, Tappi J. 83 (2000) 1–22.
[27] M. Karlsson, S. Stenström, Static and dynamic modeling of cardboard drying part 1: Theoretical model, Dry. Technol. 23 (2005) 143–163.
[28] T. Lu, S. Shen, Numerical and experimental investigation of paper drying: Heat and mass transfer with phase change in porous media, Appl. Therm. Eng. 27 (2007) 1248–1258.
[29] C.H. Heo, H. Cho, Y.-K. Yeo, Dynamic modeling of paper drying processes, Korean J. Chem. Eng. 28 (2011) 1651–1657.

[30] A. Bandyopadhyay, H. Radhakrishnan, B.V. Ramarao, S.G. Chatterjee, Moisture sorption response of paper subjected to ramp humidity changes: Modeling and experiments, Ind. Eng. Chem. Res. 39 (2000) 219–226.
[31] P.A. Marin Zapata, M. Fransen, J. ten Thije Boonkkamp, L. Saes, Coupled heat and moisture transport in paper with application to a warm print surface, Appl. Math. Model. 37 (2013) 7273–7286.
[32] G. Venditti, V. Murali, A.A. Darhuber, Inkjet printing of surfactant solutions onto thin moving porous media, Colloids Surf. A 634 (2022) 127832.
[33] K. Murugesan, K.N. Seetharamu, P.A.A. Narayana, A one dimensional analysis of convective drying of porous materials, Heat Mass Transf. 32 (1996) 81–88.
[34] S. Lavrykov, B. Ramarao, R. Solimeno, K. Singh, Analysis of heat and moisture transients in paper during copying and digital printing processes, J. Imaging Sci. Technol. 57 (2013) 060504–1–8.
[35] B. Kulkarni, H.T. Vu, E. Tsotsas, Mass and heat transport models for analysis of the drying process in porous media: A review and numerical implementation, Int. J. Chem. Eng. 2018 (2018) 9456418.
[36] V. Murali, J.C. Zeegers, A.A. Darhuber, Infrared thermography of sorptive heating of thin porous media – Experiments and continuum simulations, Int. J. Heat Mass Transfer 147 (2020) 118875.
[37] J.K. Lin, M.R. Ladisch, J.A. Patterson, C.H. Noller, Determining pore size distribution in wet cellulose by measuring solute exclusion using a differential refractometer, Biotechnol. Bioeng. 29 (1987) 976–981.
[38] R.P. Neuman, L.P. Walker, Solute exclusion from cellulose in packed columns: Experimental investigation and pore volume measurements, Biotechnol. Bioeng. 40 (1992) 218–225.
[39] G. Grznárová, S. Yu, V. Štefuca, M. Polakovič, Quantitative characterization of pore structure of cellulose gels with or without bound protein ligand, J. Chromatogr. A 1092 (2005) 107–113.
[40] Tetraethylene Glycol, The Dow Chemical Company, 2003.
[41] L. Ninni, M. Camargo, A. Meirelles, Water activity in poly(ethylene glycol) aqueous solutions, Thermochim. Acta 328 (1999) 169–176.
[42] R. Sadeghi, Y. Shahebrahimi, Vapor-liquid equilibria of aqueous polymer solutions from vapor-pressure osmometry and isopiestic measurements, J. Chem. Eng. Data 56 (2011) 789–799.
[43] J.J. van Laar, Über dampfspannungen von binären gemischen, Z. Phys. Chem. 72 (1910) 723–751.
[44] J.J. van Laar, Einiges über dampfspannungen von einheitlichen stoffen und von binären gemischen, Z. Anorg. Allg. Chem. 171 (1928) 42–60.
[45] P. Atkins, J. De Paula, Atkins' Physical Chemistry, Macmillan, 2006.
[46] E.J. Quirijns, A.J. van Boxtel, W.K. van Loon, G. van Straten, Sorption isotherms, GAB parameters and isosteric heat of sorption, J. Sci. Food Agric. 85 (2005) 1805–1814.
[47] M. Peleg, Modeling degradation kinetics in dry foods storage under varying temperature and moisture content—Theoretical evaluation, Food Eng. Rev. 11 (2019) 1–13.
[48] K.M. Rathfelder, L.M. Abriola, M.A. Singletary, K.D. Pennell, Influence of surfactant-facilitated interfacial tension reduction on chlorinated solvent migration in porous media: observations and numerical simulation, J. Contam. Hydrol. 64 (2003) 227–252.
[49] A. Ashari, H. Vahedi Tafreshi, General capillary pressure and relative permeability expressions for through-plane fluid transport in thin fibrous sheets, Colloids Surf. A 346 (2009) 114–122.
[50] G. Barenblatt, Y.P. Zheltov, I. Kochina, Basic concepts in the theory of seepage of homogeneous liquids in fissured rocks, J. Appl. Math. Mech. 24 (1960) 852–864.
[51] G.A. Gist, A.H. Thompson, A.J. Katz, R.L. Higgins, Hydrodynamic dispersion and pore geometry in consolidated rock, Phys. Fluids A 2 (1990) 1533–1544.
[52] M. Sahimi, Dispersion in flow through porous media, in: Flow and Transport in Porous Media and Fractured Rock, John Wiley & Sons, Ltd, 2011, pp. 341–413, Ch. 11.
[53] S. Khirevich, A. Höltzel, U. Tallarek, Validation of pore-scale simulations of hydrodynamic dispersion in random sphere packings, Commun. Comput. Phys. 13 (2013) 801–822.
[54] H. Hu, R.G. Larson, Evaporation of a sessile droplet on a substrate, J. Phys. Chem. B 106 (2002) 1334–1344.
[55] A. Selvadurai, Partial Differential Equations in Mechanics, Springer, 2000.
[56] C.-L. Wong, S. Wang, S. Karimnejad, M.G. Wijburg, H. Mansouri, A.A. Darhuber, Transient deformation and swelling of paper by aqueous co-solvent solutions, Soft Matter 19 (2023) 1202–1211, http://dx.doi.org/10.1039/D2SM01388F.
[57] N.A. Peppas, C.T. Reinhart, Solute diffusion in swollen membranes. Part I. A new theory, J. Membr. Sci. 15 (1983) 275–287.
[58] H. Yasuda, A. Peterlin, C.K. Colton, K.A. Smith, E.W. Merrill, Permeability of solutes through hydrated polymer membranes. Part III. Theoretical background for the selectivity of dialysis membranes, Makromol. Chem. 126 (1969) 177–186.
[59] S. Sato, S.W. Kim, Macromolecular diffusion through polymer membranes, Int. J. Pharm. 22 (1984) 229–255.
[60] M. Tokita, Transport in and through gel, in: V.K. Thakur, M.K. Thakur (Eds.), Polymer Gels: Science and Fundamentals, Springer, Singapore, 2018, pp. 413–443.
[61] A.G. Ogston, B.N. Preston, J.D. Wells, On the transport of compact particles through solutions of chain-polymers, Proc. R. Soc. Lond. A Math. 333 (1973) 297–316.
[62] R.I. Cukier, Diffusion of Brownian spheres in semidilute polymer solutions, Macromolecules 17 (1984) 252–255.
[63] C.K. Colton, K.A. Smith, E.W. Merrill, P.C. Farrell, Permeability studies with cellulosic membranes, J. Biomed. Mater. Res. 5 (1971) 459–488.
[64] D. Langevin, F. Rondelez, Sedimentation of large colloidal particles through semidilute polymer solutions, Polymer 19 (1978) 875–882.
[65] W. Brown, R. Johnsen, Diffusion in polyacrylamide gels, Polymer 22 (1981) 185–189.
[66] N. Nishioka, K. Watase, K. Arimura, K. Kosai, M. Uno, Permeability through cellulose membranes grafted with vinyl monomers in a homogeneous system I. Diffusive permeability through acrylonitrile grafted cellulose membranes, Polym. J. 16 (1984) 867–875.
[67] A. Pluen, P.A. Netti, R.K. Jain, D.A. Berk, Diffusion of macromolecules in agarose gels: Comparison of linear and globular configurations, Biophys. J. 77 (1999) 542–552.
[68] L. Nilsson, S. Stenström, A study of the permeability of pulp and paper, Int. J. Multiph. Flow 23 (1997) 131–153.
[69] B.V. Ramarao, A. Massoquete, S. Lavrykov, S. Ramaswamy, Moisture diffusion inside paper materials in the hygroscopic range and characteristics of diffusivity parameters, Dry. Technol. 21 (2003) 2007–2056.
[70] S. Lavrykov, S.K. Singh, B.V. Ramarao, S. Ramaswamy, H. Pande, Analysis of the permeability tensor and the correlation length of heterogeneities in paper using X-ray microtomography, Dry. Technol. 34 (2016) 871–882.
[71] F. Jiang, J. Weng, M. Jia, Y. Yang, X. Zhang, Microstructural model in COMSOL packages with simulation to aging behavior of paper materials, Cellulose 25 (2018) 1539–1553.
[72] M. Kabbej, V. Guillard, H. Angellier-Coussy, V. Thoury-Monbrun, N. Gontard, L. Orgéas, S. Rolland Du Roscoat, S. Gaucel, From 3D real structure to 3D modelled structure: Modelling water vapor permeability in polypropylene/cellulose composites, Polymer 269 (2023) 125672.
[73] C.I. Thomson, R.M. Lowe, A.J. Ragauskas, First characterization of the development of bleached kraft softwood pulp fiber interfaces during drying and rewetting using FRET microscopy, Holzforschung 62 (2008) 383–388, URL https://doi.org/10.1515/HF.2008.069.
[74] T. Joffre, P. Isaksson, P.J.J. Dumont, S.R.d. Roscoat, S. Sticko, L. Orgéas, E.K. Gamstedt, A method to measure moisture induced swelling properties of a single wood cell, Exp. Mech. 56 (2016) 723–733.
[75] N.H. Vonk, N.A.M. Verschuur, R.H.J. Peerlings, M.G.D. Geers, J.P.M. Hoefnagels, Robust and precise identification of the hygro-expansion of single fibers: a full-field fiber topography correlation approach, Cellulose 27 (2020) 6777–6792.
[76] N.H. Vonk, S. van Weele, G. Slokker, M.P.F.H.L. van Maris, J.P.M. Hoefnagels, Challenges and solutions of environmental scanning electron microscopy characterisation of biomaterials: Application to hygro-expansion of paper, Strain 59 (2023) e12440.